Theoret. Comput. Fluid Dynamics (1997) 9: 1–16

Theoretical and Computational Fluid Dynamics

Low-Dimensional Description of Oscillatory Thermal Convection: The Small Prandtl Number Limit[1]

H. Gunes, A. Liakopoulos, and R.A. Sahan

Department of Mechanical Engineering and Mechanics, Packard Laboratory, Lehigh University, Bethlehem, PA 18015, U.S.A.

Communicated by M.Y. Hussaini

Received 25 January 1996 and accepted 19 July 1996

Abstract. Low-dimensional models are derived for transitional, buoyancy-driven flow in a vertical channel with prescribed spatially periodic heating. Stationary characteristic structures (empirical eigenfunctions) are identified by applying proper orthogonal decomposition to numerical solutions of the governing partial differential equations. A Galerkin procedure is then employed to obtain suitable low-order dynamical models. Stability analysis of the fixed points of the low-order systems predicts conditions at the primary flow instability that are in very good agreement with direct numerical solutions of the full model. This agreement is found to hold as long as the low-order system possesses a possible Hopf bifurcation (minimum two-equation) mechanism. The effect of the number of retained eigenmodes on amplitude predictions is examined.

1. Introduction

The reduction of partial differential equations (PDEs) to minimal systems of ordinary differential equations (ODEs) has emerged as a major issue in the study of transitional and turbulent flows (Berkooz *et al*., 1993; Kirby, 1992). Low-dimensional models offer a compact description of the system dynamics and make feasible bifurcation and stability analyses of complex flows. Furthermore, they can be potentially useful in designing and testing flow control systems.

PDEs can be transformed into systems of ODEs by well-established procedures, e.g., the method of weighted residuals. This approach has been successfully used in conjunction with a variety of basis functions, e.g., splines (Liakopoulos and Hsu, 1984; Liakopoulos, 1985) or, most frequently, trigonometric functions and orthogonal polynomials (Gottlieb and Orszag, 1977). However, these methods lead to large systems of ODEs. The key to obtaining low-dimensional models is to expand the field variables in terms of basis functions that are constructed separately for each flow system and reflect its behavior in some range of the controlling dimensionless parameters. In this work we obtain an optimal basis by applying the method of Proper Orthogonal Decomposition (POD) introduced in fluid dynamics by Lumley (1967) as a tool for eddy identification in turbulent flows.

POD offers an objective method of identifying the most energetic eigenmodes, thus enabling us to compress numerical or experimental data by retaining a small number of modes that capture most of the fluctuation energy. POD methodology has been applied to a variety of problems in diverse fields such as meteorology, oceanography, pattern recognition, and psychology. Some of the specific investigations in

[1] This work was partially supported by NASA/LeRC under Contract NAG 3-1632.

fluid dynamics include: the dynamics of coherent structures in the turbulent wall layer (Aubry *et al*., 1988; Berkooz *et al*., 1993), analysis of randomly forced Burgers' equation (Chambers *et al*., 1988), dynamical eigenfunction decomposition of turbulent channel flow (Ball *et al*., 1991), and the evolution of three-dimensional coherent structures in a flat-plate boundary layer (Rempfer and Fasel, 1994). A large number of applications of POD to postprocessing and analysis of experimental data has been reported, e.g., Glauser and George (1987), Lu and Smith (1991), Rajaee *et al*. (1994). Sirovich and Rodriguez (1987) presented a POD-based reduced model for the Ginzburg–Landau equation. Deane *et al*. (1991) reported a low-dimensional model for two-dimensional isothermal flow in a grooved channel and studied the accuracy of short- and long-time model predictions through simulation, continuation, and bifurcation analysis. Sahan *et al*. (1995) developed low-order dynamical models for nonisothermal grooved channel flow. Deane and Mavriplis (1994) applied POD to the separated flow past thick airfoils and found that the mode amplitudes obtained by integration of the low-order model were considerably larger than those calculated through direct projection of the full model. They suggested that the number of snapshots and the number of retained modes were the main issues to be addressed in the future. Recently, Gunes *et al*. (1995) obtained a low-dimensional representation of transitional, buoyancy-driven air flow ($Pr = 0.71$) in a vertical channel.

In this study we apply POD methodology to oscillatory convection in a Boussinesq fluid of low Prandtl number. We consider convection in a long vertical channel with periodically spaced heaters along the left vertical wall. This configuration arises frequently in electronic equipment cooled by free convection. The spatial eigenfunctions are determined by applying the method of snapshots. A Galerkin procedure is then employed to obtain suitable low-order dynamical models. Stability analysis is performed on the derived low-dimensional models. Finally, low-order system predictions are compared with those of the full model. The limit $Pr = 0$ is examined in detail.

2. Full Model

Free convection in a Boussinesq fluid is described by the dimensionless equations

$$\nabla \cdot \vec{V} = 0, \tag{1}$$

$$\frac{\partial \vec{V}}{\partial t} + (\vec{V} \cdot \nabla)\vec{V} + \nabla P = \Theta \vec{j} + \frac{1}{\sqrt{Gr}} \nabla^2 \vec{V}, \tag{2}$$

$$\frac{\partial \Theta}{\partial t} + \vec{V} \cdot \nabla \Theta = \frac{1}{Pr\sqrt{Gr}} \nabla^2 \Theta, \tag{3}$$

where $Pr = \nu/\alpha$ denotes the Prandtl number, $Gr = \beta g q'' l^4 / \nu^2 k$ is the Grashof number, $\vec{j}$ is the unit vector in the direction opposite to the gravitational force, l is the channel width, ν is the kinematic viscosity, α is the thermal diffusivity, β is the thermal expansion coefficient, g is the acceleration of gravity, k is the thermal conductivity, and q'' denotes an applied heat flux characteristic of the problem. In (1)–(3) the dimensionless variables are

$$(x, y) = \frac{(x^*, y^*)}{l}, \qquad t = \frac{u_c}{l} t^*, \qquad \vec{V} = \frac{\vec{v}^*}{u_c}, \qquad P = \frac{p^*}{\rho u_c^2}, \quad \text{and} \quad \Theta = \frac{k}{q'' l}(T - T_b),$$

where $u_c = \sqrt{\beta g l^2 q''/k}$ and T_b is the background temperature. Note that in the limit $Pr \to 0$, the energy equation reduces to Laplace's equation

$$\nabla^2 \Theta = 0. \tag{3a}$$

We consider buoyancy-induced flow in a long vertical channel with periodically spaced heaters, flush-mounted along the left vertical channel wall. The computational domain is shown in Figure 1. Periodic boundary conditions are used so that the governing equations are solved on a single module that represents the flow far from the channel entrance.

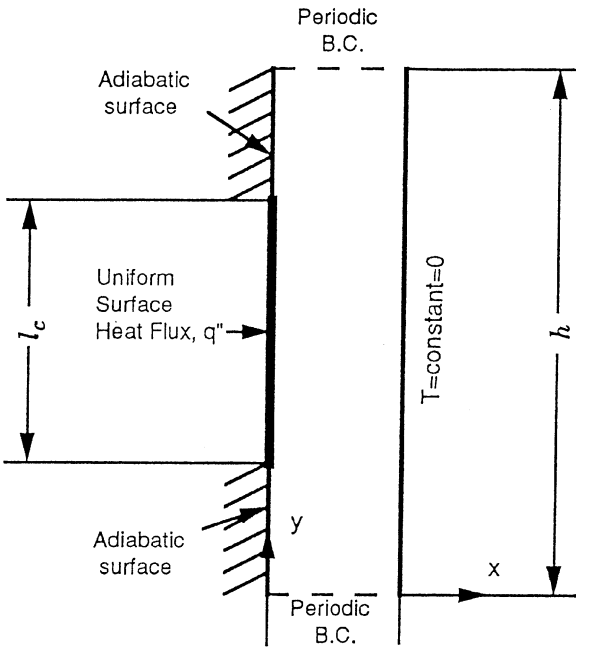

Figure 1. Computational domain. $h/l = 4$, $l_c/l = 2$, l = width of channel.

3. Construction of Low-Order Model

Following Sirovich (1987), we assume that M snapshots of the flow field have been obtained by direct numerical simulation or laboratory measurements. The velocity data are decomposed into time-averaged $(\bar{u}, \bar{v})$ and time-varying $\vec{V}' = (u', v')$ parts, and the empirical eigenfunctions are constructed as linear combinations of the time-varying velocity vector fields

$$\vec{\varphi}_k(x, y) = \sum_{i=1}^{M} \mathbf{A}_{ki} \vec{V}'_i(x, y, t_i). \tag{4}$$

In (4), $\mathbf{A}_k$ denotes the kth eigenvector of the correlation matrix $\mathbf{C}$ whose elements are

$$C_{ij} = \frac{1}{M} \int\int \vec{V}'_i(x, y, t) \vec{V}'_j(x, y, t) dx\, dy, \qquad i, j = 1, 2, \ldots, M. \tag{5}$$

By construction, $\mathbf{C}$ is an $(M \times M)$ symmetric, positive-semidefinite matrix. An eigenvalue of $\mathbf{C}$ represents the contribution of the corresponding empirical eigenfunction to the total fluctuation energy. The empirical eigenfunctions, being linear combinations of the snapshots of the flow fluctuations, are divergence-free (solenoidal) vector fields. Furthermore, the eigenfunctions form an orthogonal set and, when normalized properly $(\vec{\varphi}_i \to \vec{\varphi}_i / \sqrt{\lambda_i})$, they satisfy

$$\int\int \vec{\varphi}_i \cdot \vec{\varphi}_j dx\, dy = \delta_{ij}. \tag{6}$$

We consider next a truncated series representation of the fluctuation velocity in terms of the eigenfunctions, i.e., we write

$$\vec{V}'(x, y, t) = \sum_{k=1}^{M_1} a_k(t) \vec{\varphi}_k(x, y), \tag{7}$$

and, taking into account (6),

$$a_k(t) = \int\int \vec{V}'(x, y, t) \cdot \vec{\varphi}_k(x, y)\, dx\, dy. \tag{8}$$

In general, the number of eigenfunctions retained in the truncated series representation, M_1, is much smaller than the number of snapshots, M. The error in the reconstruction formulas, (7) and (8), vanishes as $M_1 \to M$ and the input data can be reconstructed to a desired accuracy by varying M_1.

A low-order model is derived by substituting (7) into (2), and applying the Galerkin procedure.

3.1. $Pr = 0$

For $Pr = 0$, the energy equation reduces to the steady conduction equation, (3a), and since the boundary conditions are time-independent, the temperature field is steady. Making use of the orthonormality property of the empirical eigenfunctions, we obtain a system of nonlinear ODEs for the expansion coefficients

$$\frac{da_k}{dt} = A_k + \frac{1}{\sqrt{Gr}} B_k + C_{ki} a_i + \frac{1}{\sqrt{Gr}} D_{ki} a_i + E_{kij} a_i a_j, \tag{9}$$

$k, i, j = 1, 2, \ldots, M_1$. Note that, in (9), i and j are summation indices. The coefficients appearing in (9) are related to inner products among the eigenmodes and/or mean flow and their spatial derivatives.

Note that in our approach the basis for the Galerkin procedure consists of the average velocity and the computed eigenfunctions $\vec{\varphi}_k$. The resulting ODEs contain constant terms, linear terms, and terms quadratic in a_k. A different approach has also been discussed in the literature. Starting with the Reynolds-averaged governing equations and using a form of Taylor's hypothesis, ODEs with cubic nonlinearities are obtained. For a discussion on this and other controversial modeling issues see Rempfer (1996), Berkooz *et al.* (1994), and Sirovich and Zhou (1994).

3.2. $Pr \neq 0$

When $Pr \neq 0$, temperature fluctuations are nonzero. In addition to expansion (7), we introduce a truncated series representation of the dimensionless fluctuation temperature, i.e., we write

$$\Theta'(x, y, t) = \sum_{k=1}^{M_2} b_k(t) \psi_k(x, y). \tag{10}$$

Here $\psi_k(x, y)$ denotes the kth temperature eigenfunction determined by applying POD to the temperature fluctuation data. Using expansions (7) and (10) in a Galerkin procedure we obtain $(M_1 + M_2)$ ODEs for the expansion coefficients $a_k(t)$ and $b_k(t)$:

$$\frac{da_k}{dt} = A_k + \frac{1}{\sqrt{Gr}} B_k + C_{ki} a_i + \frac{1}{\sqrt{Gr}} D_{ki} a_i + E_{kij} a_i a_j + R_{ki} b_i, \tag{11}$$

$$\frac{db_k}{dt} = F_k + \frac{1}{Pr\sqrt{Gr}} G_k + H_{ki} a_i + \frac{1}{Pr\sqrt{Gr}} I_{ki} b_i + J_{kij} a_i b_j + K_{ki} b_i.$$

4. Results for $Pr = 0$

The full mathematical model ((1), (2), and (3a)), together with the boundary conditions, was solved by a spectral element method (Nekton, 1992). In our simulations 32 two-dimensional spectral elements were used (see Figure 2). Numerical solutions were obtained for order of interpolants $N_1 = 4$, 6, 8, 10, and 12. Increasing N_1 from 8 to 10 or 12 resulted in no significant changes in the solution. Values of the field variables at representative fixed locations and integrals of the field variables over the entire domain change by less than 0.7%. The results reported in this paper were obtained for $N_1 = 8$.

The spatial eigenfunctions were determined by applying the method of snapshots to numerical solutions computed for $Gr_0 = 24{,}000$ and $Pr_0 = 0$. We refer to conditions (Pr_0, Gr_0) as "design" conditions. At these conditions, the flow field is time-dependent while the temperature field is time-independent. The time-averaged dimensionless volume flow rate is 0.333. Twenty snapshots ($M = 20$), equally spaced over one cycle, were used in the decomposition. Steady isotherms and representative instantaneous streamlines are shown in Figures 3 and 4, respectively.

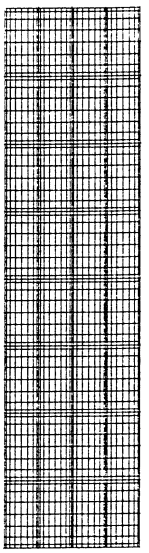

Figure 2. Computational mesh. Thirty-two spectral elements each with 9×9 collocation points.

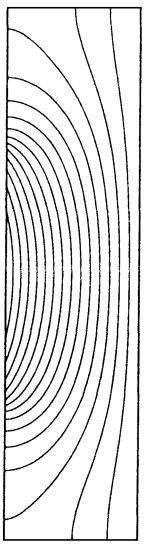

Figure 3. Steady isotherms, $Pr = Pr_0 = 0$.

The eight largest normalized eigenvalues of matrix **C** are listed in Table 1(a) together with their cumulative contribution to the total fluctuation energy. Note that the first four modes contain almost all the fluctuation energy (99.997%). The normalized empirical eigenfunctions $\vec{\varphi}_i$, $i = 1, 2, \ldots, 8$, are shown in Figure 5, and the corresponding minimum and maximum streamfunction values are listed in Table 1(b). It is clear that the most energetic modes contain the large-scale features of the flow, while modes with lower fluctuation energy levels capture smaller-scale features. Modes $(\vec{\varphi}_1, \vec{\varphi}_2)$ form a pair and are phase shifted relative to each other by $h/8$, where h is the module height defined in Figure 1. Similarly, modes $(\vec{\varphi}_3, \vec{\varphi}_4)$ form a pair, $\vec{\varphi}_4$ being approximately displaced by $h/16$ with respect to $\vec{\varphi}_3$. Within each pair, the corresponding eigenvalues are comparable in magnitude (see Table 1(a)). Higher modes come in pairs and are approximately phase-shifted versions of each other.

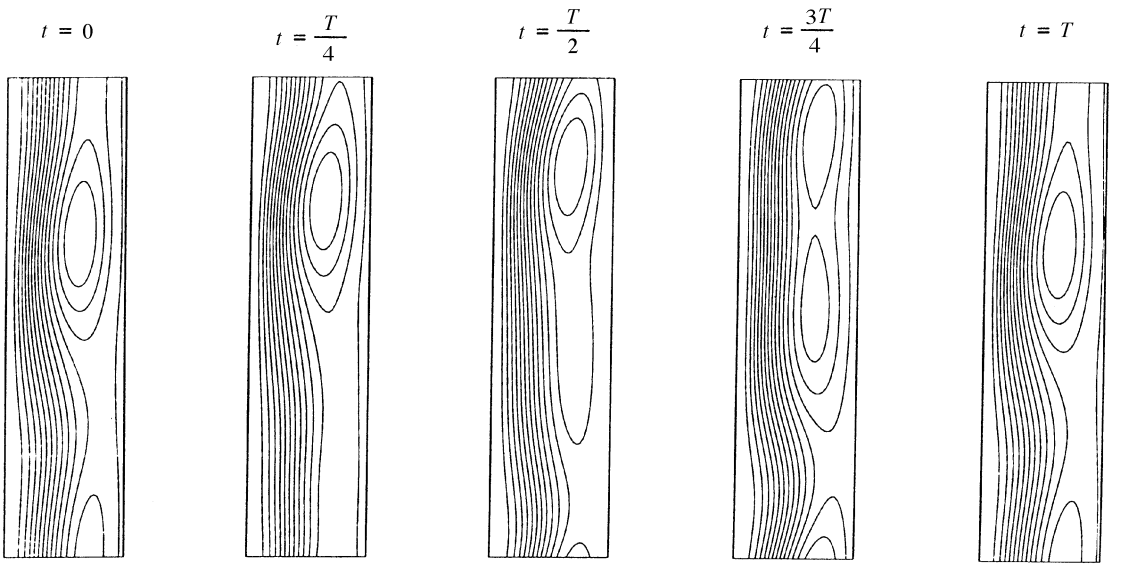

Figure 4. Instantaneous streamlines, $Gr = Gr_0 = 24{,}000$, $Pr = Pr_0 = 0$.

Table 1. (a) Normalized eigenvalues of the eight most energetic modes and their contribution to the total fluctuation energy, $Gr_0 = 24{,}000$, $Pr_0 = 0$.

Mode	Normalized eigenvalue	Cumulative energy contribution (%)
1	0.54427	54.427
2	0.45022	99.449
3	0.00303	99.752
4	0.00245	99.997
5	0.182×10^{-4}	99.998
6	0.140×10^{-4}	99.999
7	0.206×10^{-6}	99.999
8	0.156×10^{-6}	99.999

(b) Normalized empirical eigenfunctions. Maximum and minimum streamfunction values, $Gr_0 = 24{,}000$, $Pr_0 = 0$.

	$\vec{\varphi}_1$	$\vec{\varphi}_2$	$\vec{\varphi}_3$	$\vec{\varphi}_4$	$\vec{\varphi}_5$	$\vec{\varphi}_6$	$\vec{\varphi}_7$	$\vec{\varphi}_8$
Maximum	0.224	0.219	0.228	0.198	0.155	0.168	0.159	0.161
Minimum	−0.220	−0.233	−0.224	−0.243	−0.180	−0.170	−0.154	−0.160

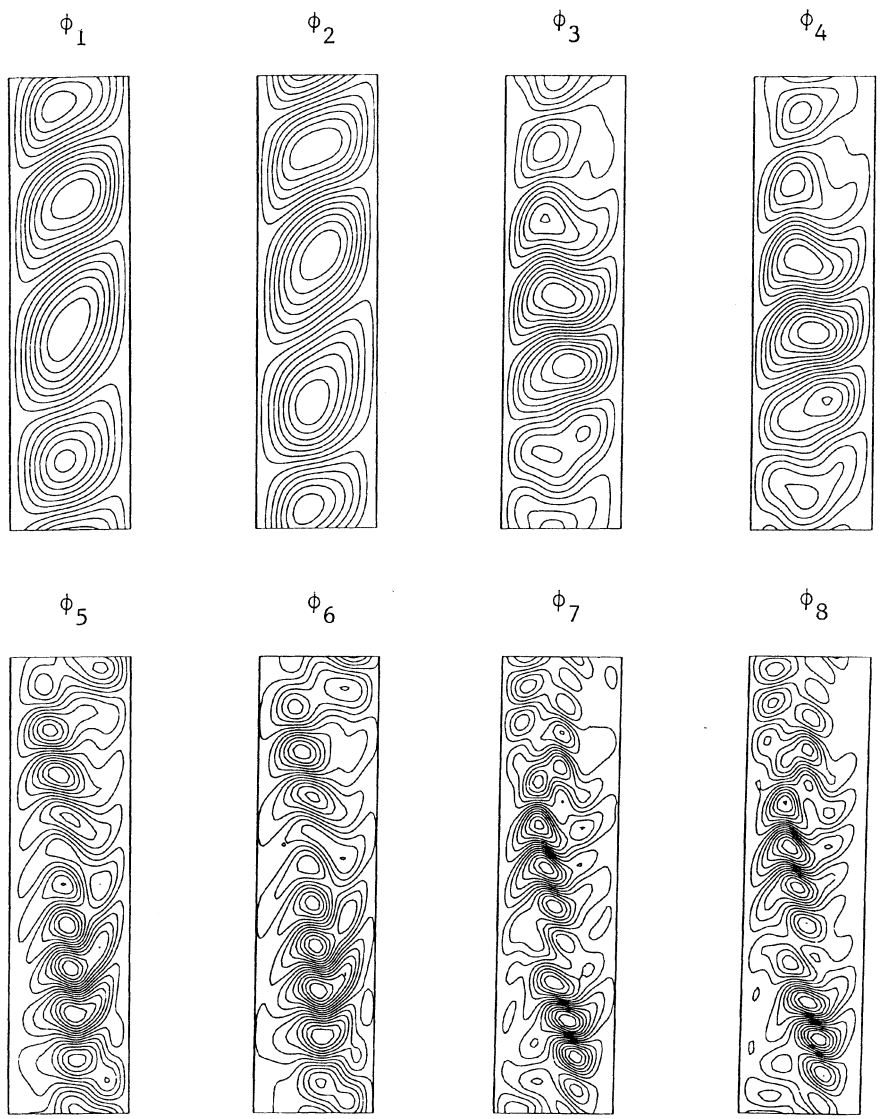

Figure 5. Empirical eigenfunctions (streamlines), $Gr_0 = 24{,}000$, $Pr_0 = 0$.

It should be noted that although the calculation of the most energetic eigenfunctions is a robust numerical procedure, higher-order eigenfunctions are sensitive to the numerical implementation of POD and to numerical parameters such as spatial resolution of the input data, number of snapshots, etc. For example, in the problem at hand, carrying out the required integrations by conventional quadrature methods (trapezoidal rule, Simpson rule, etc.) instead of using Gauss quadrature on the Gauss–Legendre–Lobatto nodes on which the input data are known, affects considerably the eigenfunctions $\vec{\varphi}_k$, $k > 4$. In contrast, eigenfunctions $\vec{\varphi}_1, \vec{\varphi}_2, \ldots, \vec{\varphi}_4$ remain unaffected.

4.1. Low-Order Models: Performance at "Design" Conditions

In this section we discuss the effect of M_1 on the low-order model predictions at "design" conditions ($Gr_0 = 24{,}000$, $Pr_0 = 0$). As expected, it is necessary to include a minimum number of eigenmodes in the low-order model. Retaining fewer modes in the truncated series expansion either does not produce stable oscillations in time or fails to predict the correct amplitude of the oscillation. For the problem at hand, at least three (the most dominant) modes are needed in order to obtain a time-dependent solution at design conditions. However, the amplitudes of the expansion coefficients predicted by the low-order model for $M_1 = 3$, are much larger than the expansion coefficients calculated by the reconstruction formula, (8), using the numerical simulation data (see Figure 6). Table 2(a) lists the amplitude (mean value to peak value) of $a_1(t)$ as a function of M_1. It is seen that the four-equation model gives the most accurate prediction of the amplitude of oscillations at design conditions. For $M_1 > 4$, the accuracy of the amplitude prediction decreases due to the noise present in the higher modes. In contrast, the frequency content of the expansion coefficients obtained by numerical integration of the low-order model is in very good agreement with the direct projection results as long as $M_1 \geq 3$.

In the remainder of this section we present results based on the four-equation model. The system of ODEs for $M_1 = 4$ is given explicitly in Appendix 1. The variation of expansion coefficients, a_i, $i = 1, 2, \ldots, 4$, with time is shown in Figure 7. In Figure 7 only the long-time behavior is shown, i.e., solutions are plotted after all initial transients have died out. The periodic character of the low-order model solutions for $t \to \infty$ is evident in Figure 8, where trajectories are plotted in the state-space domain and the short-time predictions of the low-order model are contrasted with the long-time predictions. Full model solution data were used in (8) to generate the initial conditions for the expansion coefficients. As time progresses, the amplitudes of the expansion coefficients increase slightly until a limit cycle is reached. The accuracy of the four-equation model long-time prediction of the oscillation amplitude is excellent when compared with the direct projection of the snapshots on the eigenfunctions shown in Figure 7.

The dominant dimensionless frequencies of the expansion coefficients obtained by fast Fourier transform are listed in Table 3. Coefficients a_1 and a_2 have the same fundamental frequency of oscillation ($f^0 = 0.145$) and they are phase shifted by $T^0/4$. Similarly, a_3 and a_4 have the same frequency content ($f^0 = 0.145$ and a much stronger first harmonic $f^1 = 2f^0 = 0.290$), but they are phase shifted by $T^1/4 = T^0/8$. Since the corresponding spatial modes $(\vec{\varphi}_1, \vec{\varphi}_2)$ and $(\vec{\varphi}_3, \vec{\varphi}_4)$ are also out of phase, the flow pattern is a traveling wave, i.e., the combination (a_1, a_2) with $(\vec{\varphi}_1, \vec{\varphi}_2)$ corresponds to a dynamical "coherent structure" of the velocity field.

4.2. Stability Analysis

Equation (9) is of the form

$$\frac{da_k}{dt} = F_k(a_1, a_2, \ldots, a_{M_1}, Gr), \qquad k = 1, 2, \ldots, M_1. \tag{12}$$

Setting $F_k = 0$ in (12) and numerically solving the resulting nonlinear algebraic equations, we obtain the equilibrium points

$$a_k = f_k(Gr), \qquad k = 1, 2, \ldots, M_1. \tag{13}$$

The stability of a fixed point is governed by the eigenvalues of the associated Jacobian matrix, J, evaluated at the fixed point. Note that the Jacobian matrix of the low-dimensional system, (9), is real and

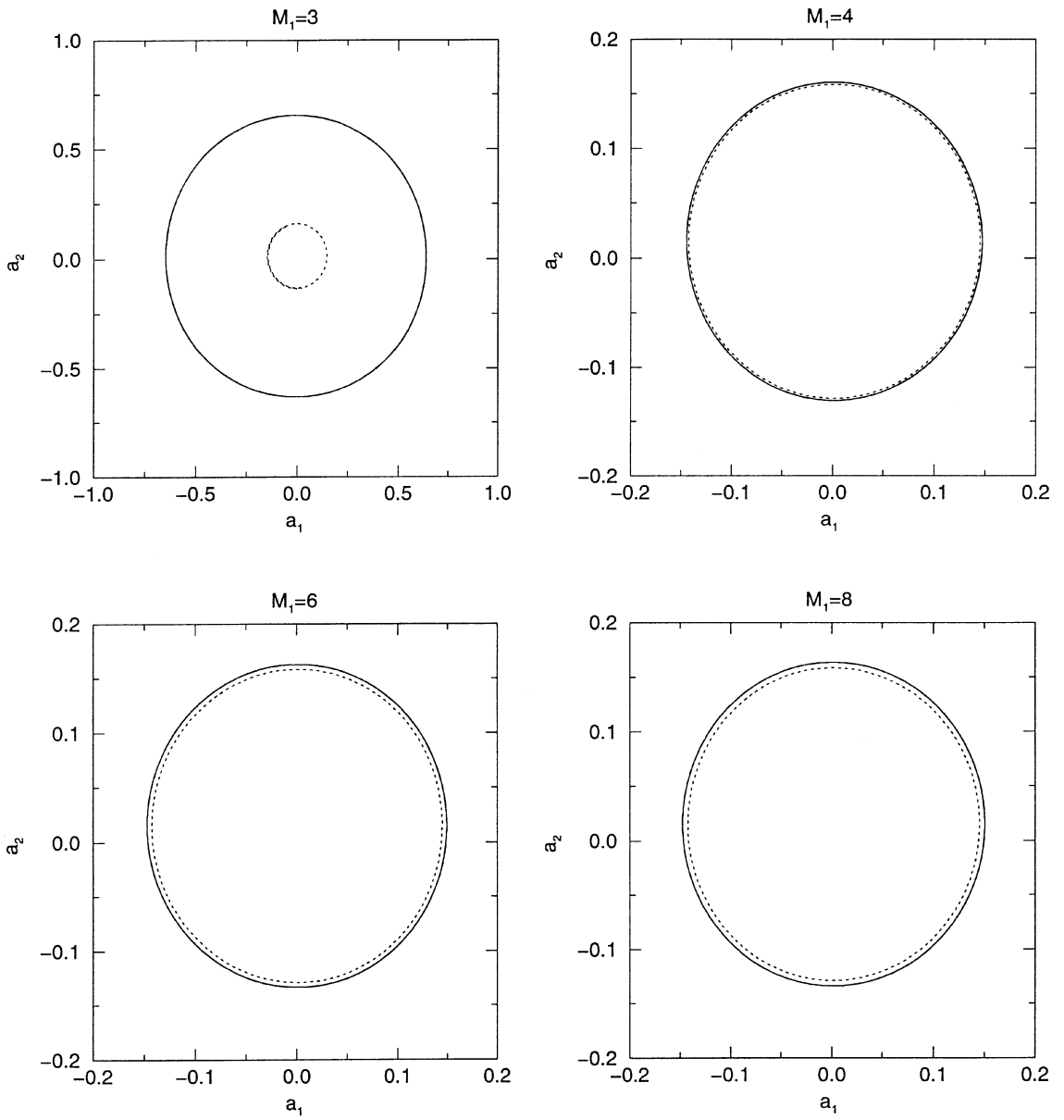

Figure 6. Effect of number of retained modes M_1 on temporal expansion coefficients. Solid line: low-order model; dotted line: direct projection of snapshots on the eigenfunctions. $Gr_0 = 24{,}000$, $Pr_0 = 0$.

nonsymmetric. We have studied the stability of fixed points of the low-order models obtained for $M_1 = 4$ and 8. For Gr smaller than a critical Grashof number, Gr_c, the real parts of all eigenvalues of J are negative leading to stable fixed points, i.e., for $Gr < Gr_c$ the steady solutions of (9) are immune to small disturbances to initial conditions. This is in agreement with the full model ((1), (2), and (3a)) which has a unique stable steady solution for low values of Grashof number. In Table 2(b) we list the conditions at the onset of primary instability as predicted by low-order models for $M_1 = 4$ and 8. Both models predict a Hopf bifurcation (i.e., an equilibrium point becomes unstable and a stable limit cycle emerges) at $Gr_c = 23{,}200$. This is in very good agreement with the critical Grashof number predicted by the full model. Direct numerical simulations based on (1), (2), and (3a) predict that the flow becomes time-periodic at about $Gr \simeq 2.3 \times 10^4$. It is interesting to note that even though the two-equation model is not adequate to describe

Table 2. (a) Amplitude of $a_1(t)$ as function of M_1. Full model prediction = 0.142. $Gr_0 = 24{,}000$, $Pr_0 = 0$.

M_1	Amplitude of expansion coefficient, a_1
2	Fails to predict periodic oscillations
3	0.700
4	0.143
6	0.150
8	0.151
10	0.165
12	0.400

(b) Conditions at the onset of primary instability as predicted by two low-order models, $Gr_0 = 24{,}000$, $Pr_0 = 0$.

M_1	Gr_c	Fundamental angular frequency, $\omega^0 = 2\pi f^0$
4	23,200	0.919
8	23,200	0.919

the flow dynamics at design conditions, it predicts the onset of first instability (Hopf bifurcation) accurately. The frequency of oscillations at the onset of temporal instability is predicted through stability analysis by both models to be $\omega^0 = 0.919$ which corresponds to $f^0 = \omega^0/2\pi = 0.146$. This is in very good agreement with both the direct numerical solution of the full model and the numerical integration of the low-order models (see Section 4.1).

A complete bifurcation analysis of the low-order models is beyond the scope of this paper. Instead, we have obtained several numerical solutions of the four-equation model for various values of $Gr > Gr_c$. Trajectories in the state-space domain for $Gr = 2.35 \times 10^5$ are shown in Figure 9. Increasing Gr further, leads to chaotic behavior.

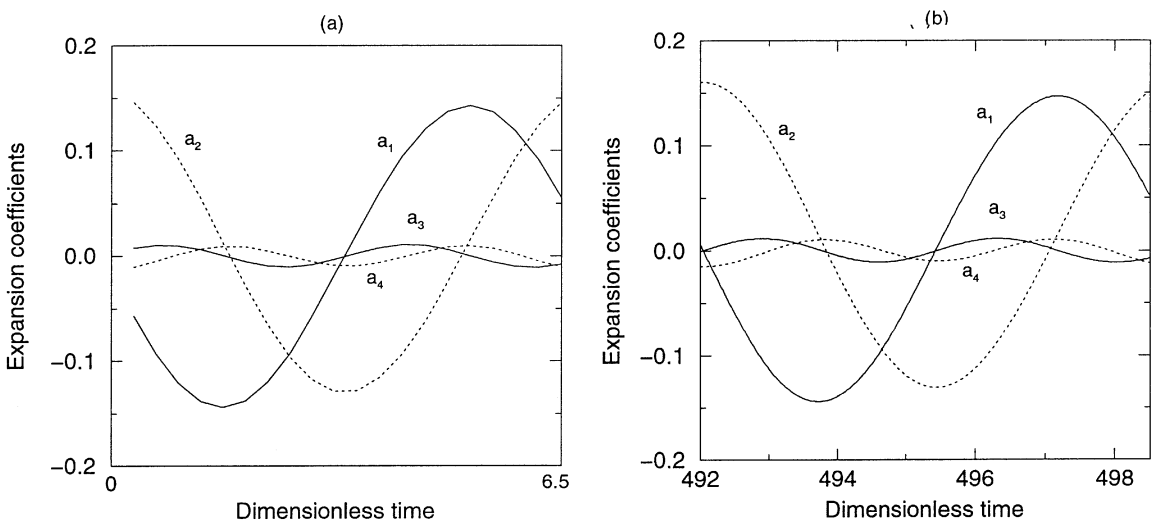

Figure 7. Temporal expansion coefficients. (a) Direct projection of snapshots on the eigenfunctions. (b) Low-order model, $M_1 = 4$. $Gr_0 = 24{,}000$, $Pr_0 = 0$.

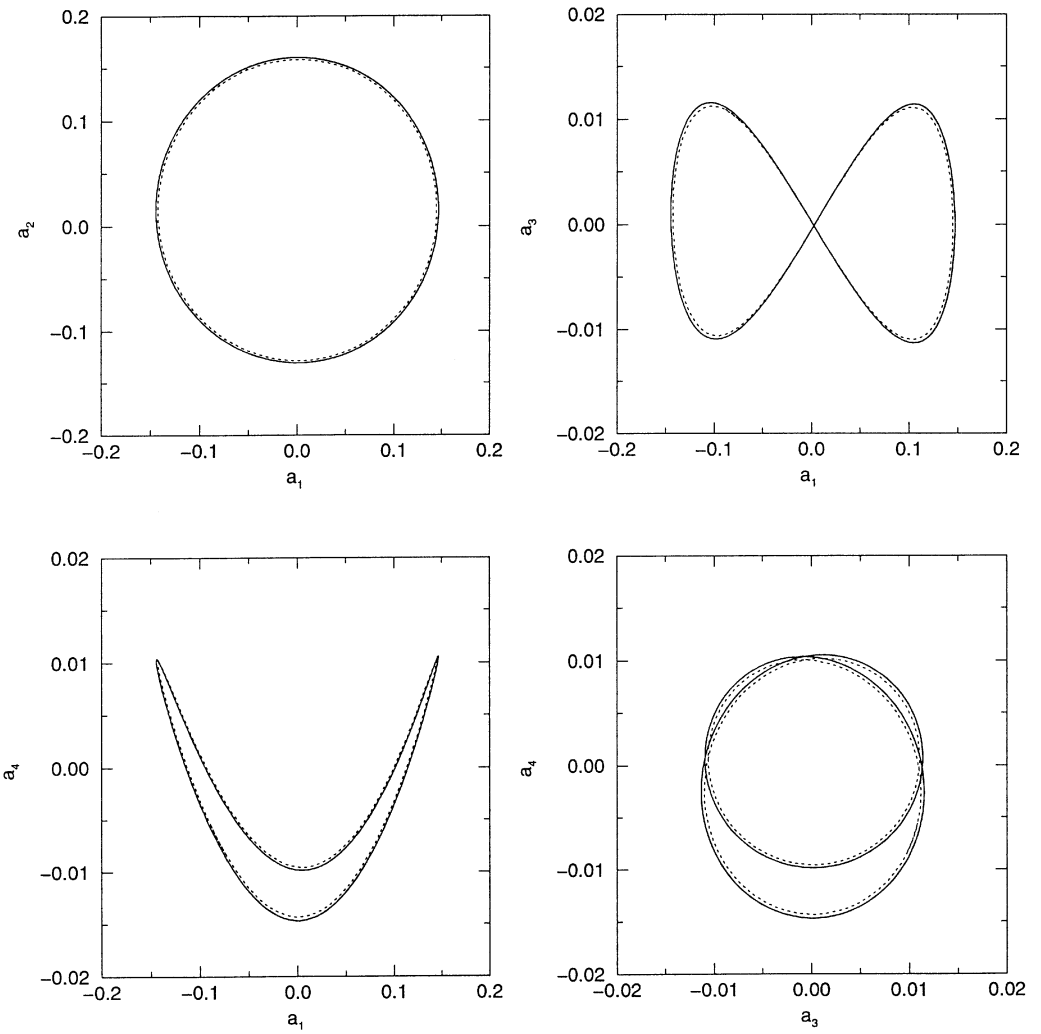

Figure 8. Trajectories in the state-space domain, low-order model, $M_1 = 4$. $Gr_0 = 24{,}000$, $Pr_0 = 0$. Solid line: long-term dynamics; dotted line: short-term dynamics.

Table 3. Dominant frequency and amplitude of the expansion coefficients $a_i(t)$. Low-order model, $Gr_0 = 24{,}000$, $Pr_0 = 0$, $M_1 = 4$.

a_i	Dimensionless frequency, f	Amplitude
a_1	0.145	0.657×10^{-1}
a_2	0.145	0.653×10^{-1}
a_3	0.290	0.367×10^{-2}
a_4	0.290	0.367×10^{-2}

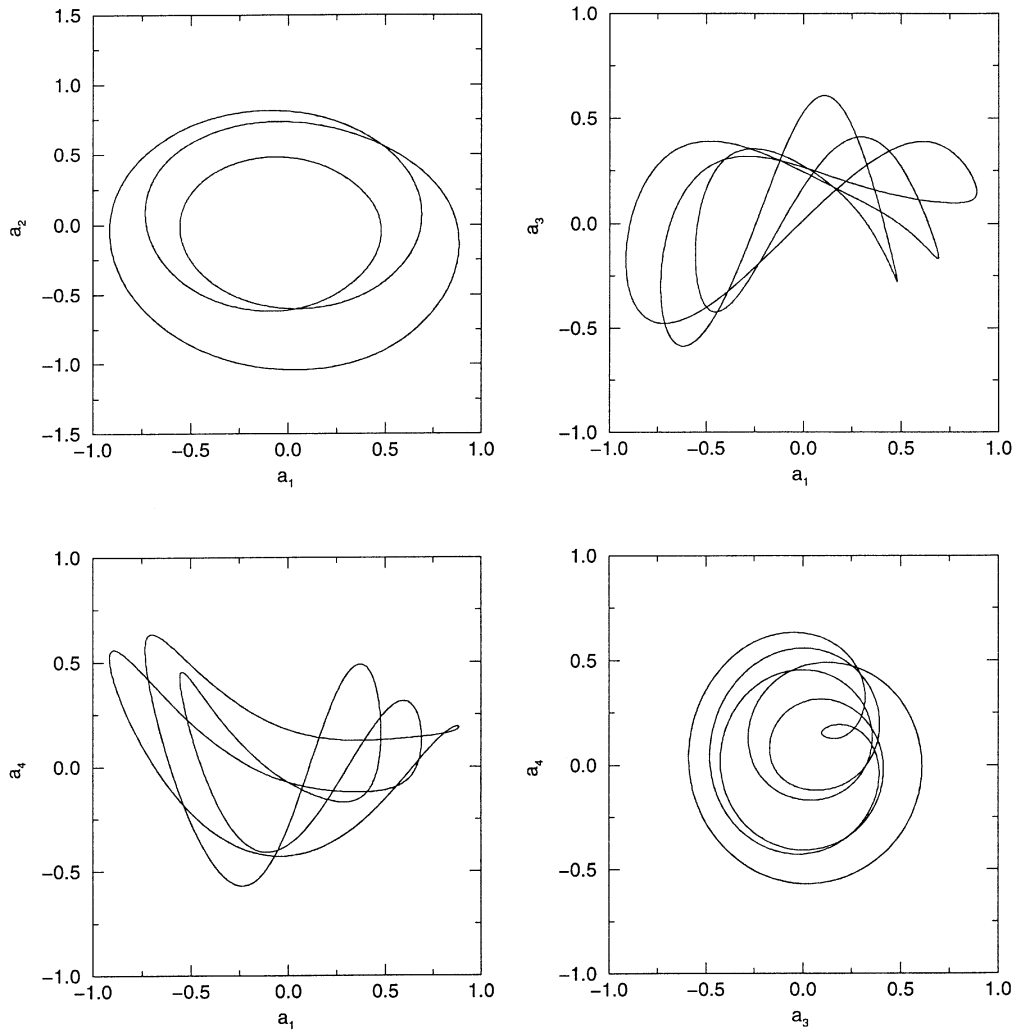

Figure 9. Trajectories in the state-space domain for $Gr = 2.35 \times 10^5$ and $Pr = 0$ based on the low-order model developed for $Gr_0 = 24{,}000$, $Pr_0 = 0$, $M_1 = 4$.

5. Results for $Pr \neq 0$

The method of analysis described in the previous sections was applied to spectral element solutions of (1), (2), and (3) computed for $Pr_0 = 0.1$ and $Gr_0 = 22{,}000$. The time-averaged dimensionless volume flow rate is 0.264. For these values of the controlling dimensionless parameters the flow and temperature fields are time-dependent.

The eight largest normalized eigenvalues for velocity and temperature are listed in Table 4, while the corresponding normalized velocity ($\vec{\varphi}_k, k = 1, 2, \ldots, 8$) and temperature ($\psi_k, k = 1, 2, \ldots, 8$) eigenfunctions are shown in Figures 10 and 11, respectively. All eigenfunctions and eigenvalues appear in pairs and within each pair the eigenfunctions are displaced relative to each other. Furthermore, the corresponding temporal coefficients $a_k(t)$ and $b_k(t)$ are displaced by a quarter period leading to the conclusion that each spatiotemporal pair corresponds to a traveling wave. Temporal expansion coefficients at design conditions are presented in Figure 12 in the state-space domain. The agreement between the results from direct projection of snapshots on the eigenfunctions and from the dynamical equation for $M_1 = M_2 = 4$ is very good.

Table 4. Normalized eigenvalues of the eight most energetic modes and their contribution to the total fluctuation "energy", $Gr_0 = 22{,}000$, $Pr_0 = 0.1$.

Mode	(a) Velocity		(b) Temperature	
	Normalized eigenvalue	Cumulative energy contribution (%)	Normalized eigenvalue	Cumulative energy contribution (%)
1	0.49837	49.837	0.50412	50.412
2	0.49492	99.329	0.49517	99.929
3	0.00334	99.663	0.000350	99.964
4	0.00332	99.995	0.000345	99.998
5	0.193×10^{-4}	99.996	0.525×10^{-5}	99.999
6	0.191×10^{-4}	99.998	0.520×10^{-5}	99.999
7	0.256×10^{-6}	99.999	0.960×10^{-8}	99.999
8	0.255×10^{-6}	99.999	0.950×10^{-8}	99.999

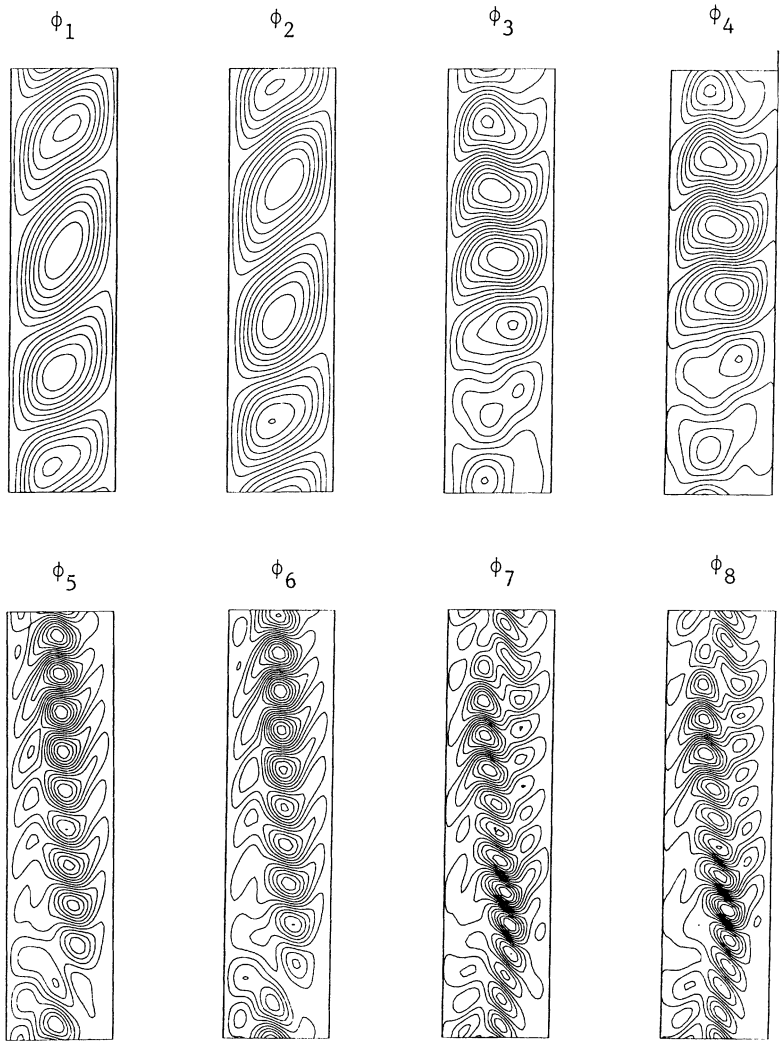

Figure 10. Velocity empirical eigenfunctions (streamlines), $Gr_0 = 22{,}000$, $Pr_0 = 0.1$.

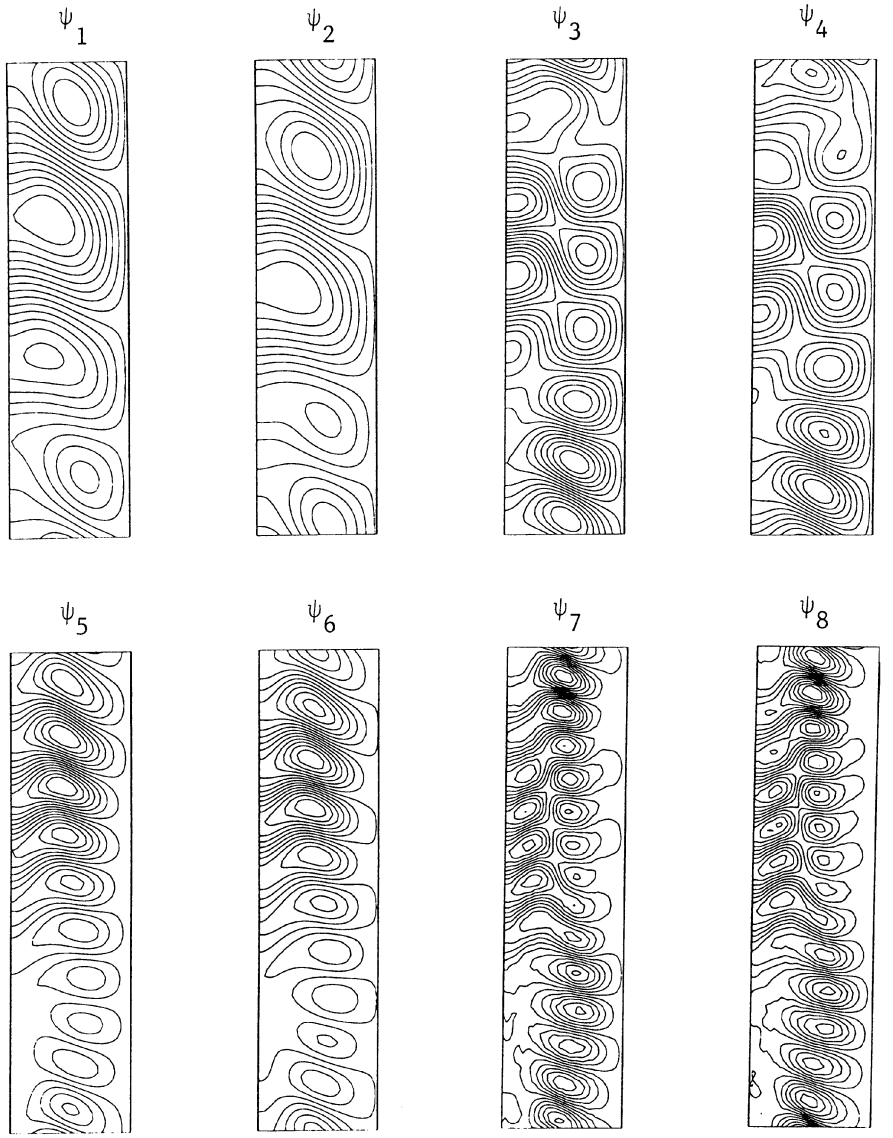

Figure 11. Temperature empirical eigenfunctions (isotherms), $Gr_0 = 22{,}000$, $Pr_0 = 0.1$.

Stability analysis of the fixed points of the low-order system has been carried out for $M_1 = M_2 = 4$. The results are summarized in Figure 13 where the solution norm $\sqrt{(a_i a_i + b_i b_i)/(M_1 + M_2)}$ is plotted against Gr. Thick lines represent stable equilibrium points (stable steady solutions) while thin lines represent unstable equilibrium points. The low-order model predicts a Hopf bifurcation at $Gr_c = 2.15 \times 10^4$. Note that direct numerical simulation based on (1), (2), and (3) predict that the flow becomes time-periodic at $Gr \simeq 2 \times 10^4$.

6. Conclusions

We have derived low-order models for transitional buoyancy-induced flow in a vertical channel with prescribed spatially periodic heating. Two Boussinesq fluids ($Pr = 0$ and $Pr = 0.1$) were considered. For this

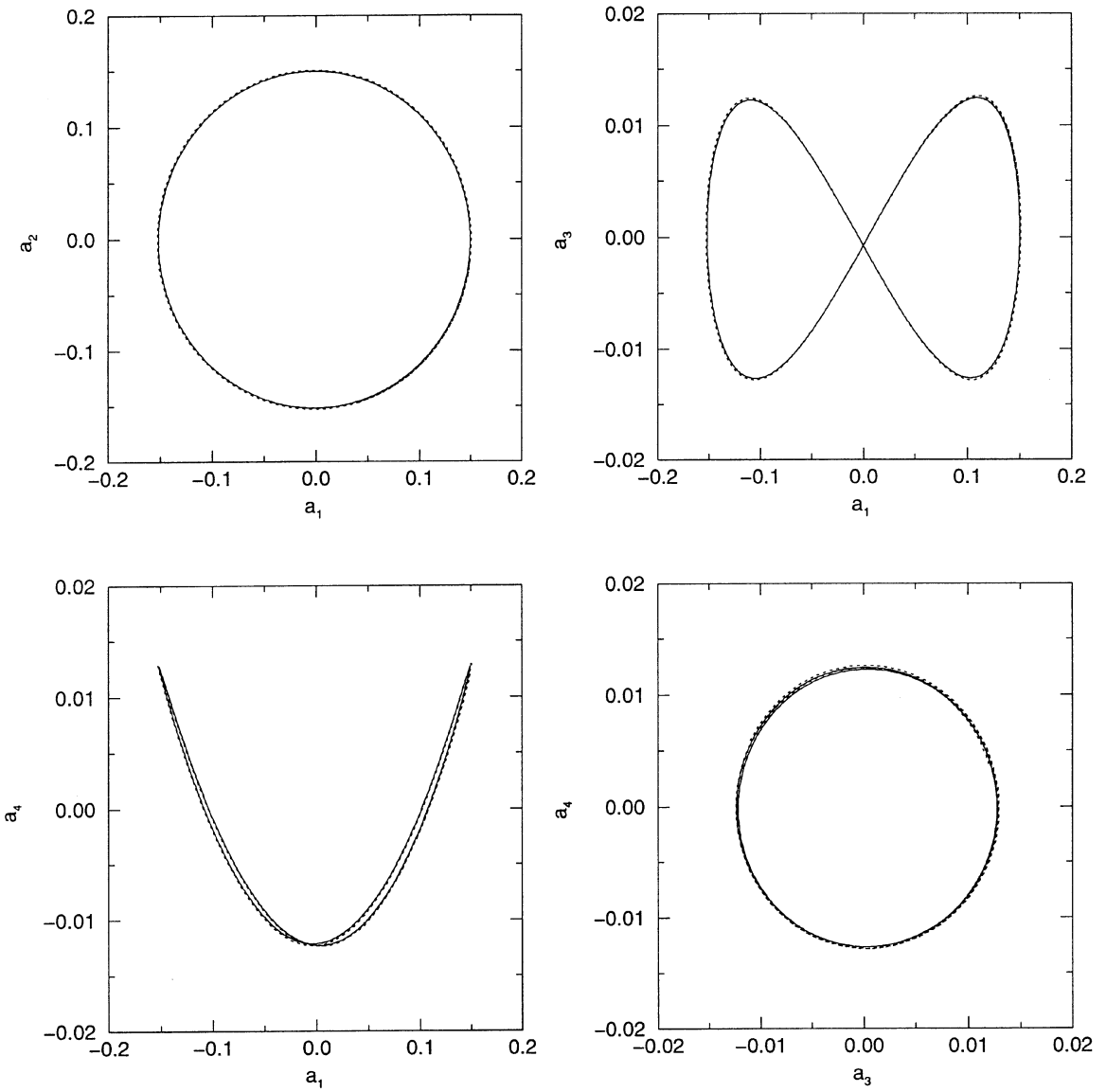

Figure 12. Trajectories in the state-space domain. Solid line: low-order model, $Gr_0 = 22{,}000$, $Pr_0 = 0.1$, $M_1 = M_2 = 4$; dotted line: direct projection of snapshots on the eigenfunctions.

problem, POD methodology gives suitable characteristic stationary structures (empirical eigenfunctions), and in conjunction with the Galerkin technique enables us to construct accurate low-order models. The empirical eigenfunctions were also found useful in identifying objective dynamical coherent structures when properly combined.

At "design" conditions, the low-order models predict satisfactorily the amplitude and frequency of oscillations of the temporal expansion coefficients. Increasing the number of equations does not necessarily lead to an improved amplitude prediction due to the inevitable noise present in the higher eigenfunctions that enter the calculations.

Stability analysis of the fixed points of the low-order systems predicts conditions at the primary flow instability that are in good agreement with direct numerical solutions of the full model. This agreement is found to hold as long as the low-order system possesses a possible Hopf bifurcation (minimum two-equation) mechanism. The frequency of oscillations predicted at critical and slightly supercritical conditions by the low-order models is in excellent agreement with the full model predictions.

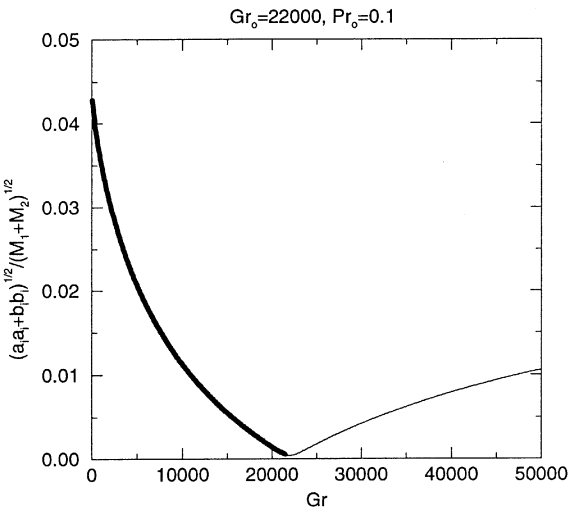

Figure 13. Norm of equilibrium points (steady solutions) as function of Grashof number. Low-order model, $Gr_0 = 22{,}000$, $Pr_0 = 0.1$, $M_1 = M_2 = 4$. Thick line: stable fixed points; thin line: unstable fixed points.

Appendix 1

Low-order model, (9) with $M_1 = 4$. $Gr_0 = 2.4 \times 10^4$, $Pr_0 = 0$, dimensionless time-averaged volume flow rate = 0.333.

$$\frac{da_1}{dt} = 0.370a_1 - 0.916a_2 - 0.0765a_3 + 0.121a_4 + \frac{-57.0a_1 - 0.0566a_2 + 3.72a_3 + 0.407a_4}{\sqrt{Gr}}$$
$$+ 0.230 \times 10^{-6}a_1^2 - 0.00753a_2a_1 - 0.0533a_3a_1 - 0.285a_4a_1 - 0.00172a_2^2 + 0.275a_3a_2$$
$$- 0.0580a_4a_2 - 0.0858a_3^2 + 0.0033a_4a_3 - 0.0841a_4^2 + 0.629\frac{1}{\sqrt{Gr}} + 0.0087,$$

$$\frac{da_2}{dt} = 0.920a_1 + 0.369a_2 - 0.0778a_3 - 0.0799a_4 + \frac{-0.0558a_1 - 56.7a_2 - 0.441a_3 + 3.24a_4}{\sqrt{Gr}}$$
$$+ 0.00753a_1^2 + 0.00172a_2a_1 + 0.290a_3a_1 - 0.0475a_4a_1 + 0.170 \times 10^{-6}a_2^2 + 0.0562a_3a_2$$
$$+ 0.284a_4a_2 + 0.0934a_3^2 + 0.0004a_4a_3 + 0.0850a_4^2 - 0.660\frac{1}{\sqrt{Gr}} + 0.0024,$$

$$\frac{da_3}{dt} = -0.0166a_1 - 0.0250a_2 + 0.0217a_3 - 1.92a_4 + \frac{3.71a_1 - 0.439a_2 - 85.8a_3 + 0.143a_4}{\sqrt{Gr}}$$
$$+ 0.0533a_1^2 - 0.565a_2a_1 + 0.0858a_3a_1 - 0.0549a_4a_1 - 0.0562a_2^2 - 0.0934a_3a_2$$
$$- 0.0744a_4a_2 - 0.296 \times 10^{-5}a_3^2 + 0.0234a_4a_3 - 0.0226a_4^2 + 0.166\frac{1}{\sqrt{Gr}} - 0.00238,$$

$$\frac{da_4}{dt} = -0.0179a_1 - 0.0223a_2 + 1.92a_3 + 0.0239a_4 + \frac{0.396a_1 + 3.23a_2 + 0.130a_3 - 85.7a_4}{\sqrt{Gr}}$$
$$+ 0.285a_1^2 + 0.106a_2a_1 + 0.0516a_3a_1 + 0.0841a_4a_1 - 0.284a_2^2 + 0.0740a_3a_2$$
$$- 0.0850a_4a_2 - 0.0234a_3^2 + 0.0226a_4a_3 - 0.900 \times 10^{-6}a_4^2 - 0.490\frac{1}{\sqrt{Gr}} + 0.00240.$$

References

Aubry, N., Holmes, P., Lumley, J.L., and Stone, E. (1988). The dynamics of coherent structures in the wall region of a turbulent boundary layer. *J. Fluid Mech.*, **192**, 115–173.

Ball, K.S., Sirovich, L., and Keefe, L.R. (1991). Dynamical eigenfunction decomposition of turbulent channel flow. *Internat. J. Numer. Methods Fluids*, **12**, 585–604.

Berkooz, G., Holmes, P., and Lumley, J.L. (1993). On the relation between low-dimensional models and the dynamics of coherent structures in the turbulent wall layer. *Theoret. Comput. Fluid Dynamics*, **4**, 255–269.

Berkooz, G., Holmes, P., Lumley, J.L., Aubry, N., and Stone, E. (1994). Observations regarding "Coherence and chaos in a model of turbulent boundary layer" by X. Zhou and L. Sirovich. *Phys. Fluids A*, **6**, 1574–1578.

Chambers, D.H., Adrian, R.J., Moin, P., Stewart, D.S., and Sung, H.J. (1988). Karhunen–Loeve expansion of Burgers' model of turbulence. *Phys. Fluids*, **31**(9), 2573–2582.

Deane, A.E., and Mavriplis, C. (1994). Low-dimensional description of the dynamics in separated flow past thick airfoils. *AIAA J.*, **32**(6), 1222–1227.

Deane, A.E., Kevrekidis, I.G., Karniadakis, G.E., and Orszag, S.A. (1991). Low-dimensional models for complex geometry flows: application to grooved channels and circular cylinders. *Phys. Fluids A*, **3**, 2337–2354.

Glauser, M.N., and George, W.K. (1987). Orthogonal decomposition of the axisymmetric jet mixing layer including azimuthal dependence. In *Advances in Turbulence* (G. Comte-Bellot and J. Mathieu, eds.), Springer-Verlag, New York.

Gottlieb, D., and Orszag, S.A. (1977). *Numerical Analysis of Spectral Methods.* Society for Industrial and Applied Mathematics, Philadelphia, PA.

Gunes, H., Sahan, R.A., and Liakopoulos, A. (1995). Low-dimensional representation of transitional buoyancy-driven flow in a vertical channel with discrete heaters. *Proc. of the* 1995 *National Heat Transfer Conference*, vol. 1 (A. Ortega and S.P. Mulay, eds.), pp. 125–137, ASME Press.

Kirby, M. (1992). Minimal dynamical systems from PDEs using Sobolev eigenfunctions. *Phys. D*, **57**, 466–475.

Liakopoulos, A. (1985). Computation of high-speed turbulent boundary-layer flows using the k–ε turbulence model. *Internat. J. Numer. Methods Fluids*, **5**(1), 81–97.

Liakopoulos, A., and Hsu, C.C. (1984). On a class of compressible laminar boundary-layer flows and the solution behavior near separation. *J. Fluid Mech.*, **149**, 339–353.

Lu, L.J., and Smith, C.R. (1991). Velocity profile reconstruction using orthogonal decomposition. *Experiments in Fluids*, **11**, 247–254.

Lumley, J.L. (1967). The structure of inhomogeneous turbulent flows. In *Atmospheric Turbulence and Radio Wave Propagation* (A.M. Yaglom and V.I. Tatarski, eds.), pp. 166–178, Nauka, Moskow.

Nekton, 1992, User's Manuals.

Rajaee, M., Karlsson, S.K.F., and Sirovich, L. (1994). Low-dimensional description of free-shear-flow coherent structures and their dynamical behaviour. *J. Fluid Mech.*, **258**, 1–29.

Rempfer, D (1996). Investigations of boundary layer transition via Galerkin projections on empirical eigenfunctions. *Phys. Fluids A*, **8**(1), 175–188.

Rempfer, D., and Fasel, H.F. (1994). Evolution of three-dimensional coherent strutures in a flat-plate boundary layer. *J. Fluid Mech.*, **260**, 351–375.

Sahan, R.A., Gunes, H., and Liakopoulos, A. (1995). Low-dimensional models for coupled momentum and energy transport problems. *Proc. of the* 1995 *International Mechanical Engineering Congress*, HTD-vol. 319/EEP-Vol. 15 (C. Amon., ed.), pp. 1–15, ASME Press.

Sirovich, L. (1987). Turbulence and the dynamics of coherent structures, Parts I–III. *Quart. Appl. Math.*, **45**(3), 561–590.

Sirovich, L., and Rodriguez, D. (1987). Coherent structures and chaos: a model problem. *Phys. Lett. A*, **120**(5), 211–214.

Sirovich, L., and Zhou, X. (1994). Reply to "Observations regarding coherence and chaos in a model of turbulent boundary layer" by X. Zhou and L. Sirovich. *Phys. Fluids A*, **6**, 1579–1582.